

Two-dimensional mapping of sea-ice keels with airborne electromagnetics

Guimin Liu* and Alex Becker*

ABSTRACT

Airborne electromagnetic (AEM) equipment can be used to sense sea ice thickness by interpreting the AEM data to obtain the distance from the towed bird that holds the EM system to the ice/seawater interface. The ice thickness itself is obtained by subtracting from that quantity the distance from the bird to the upper ice surface, as determined by a laser altimeter. To interpret AEM data acquired over sea-ice keels, we first solve the forward problem using an integral equation approach to the Neumann boundary-value problem. In this approach, we assume that sea ice is an insulator and that seawater is a perfect conductor. When the ice keel is two-dimensional, the pertinent equations can be transformed into the wavenumber domain along the strike direction, resulting in the rapid numerical computation of the AEM response. By compiling numerical-model results, we constructed an interpretation chart that relates the parameters of the observed AEM response anomaly to the geometric variables of the ice keel. The strike length of the ice keel should be about three times the bird height above the ice-water interface, so that the assumption of two-dimensionality holds. The use of the chart has been verified by interpreting field AEM data.

INTRODUCTION

The accurate measurement of floating-ice thickness has been a matter of considerable interest to the scientific community for many years (Harwood, 1971). In general, this parameter is of great importance for global climatic studies. On a more limited scale, it is a factor in the safe and efficient operation of icebreakers and other shipping. Finally, on a local scale, knowledge of the sea-ice thickness and its distribution is of vital importance in the planning and instal-

lation of oil-well drilling platforms. Because of widespread interest in this problem, possible means for effecting a remote measurement of sea-ice thickness have been the subject of periodic reviews. All of these, including a recent one prepared by Canpolar Consultants (1985 report prepared for the Canadian Department of Fisheries and Oceans), have indicated that the required measurements can be made either with low-frequency radar or with a conventional airborne electromagnetic (AEM) exploration system. Of the two, the latter is clearly preferable, because the radar measurement is susceptible to large errors where the sea ice is inhomogeneous (Rossiter and Lalumiere, 1988, Canpolar Associates report prepared for Canadian Transportation Development Center).

It appears that a confidential proposal to use airborne electromagnetics for ice thickness determination was lodged with the U.S. Navy as early as 1968 (Kovacs et al., 1987b). That proposal and other studies that followed (e.g., Becker et al., 1983; Holladay et al., 1986) clearly indicated that no difficulties were to be anticipated in obtaining the thickness of sea ice in areas where the ice-water interface was flat. Kovacs et al. (1987b) reported the results of a test on Prudhoe Bay, Alaska, which was done over an ice floe where the ice thickness varied from about 2 to 6 m over a traverse distance of about 250 m; the true average ice and snow thickness of 3.62 m was recovered from the airborne data with an accuracy of about 50 cm or roughly 15%. It is worthwhile to note that the largest error in the ice-thickness estimation was made over an ice keel which had an average thickness of about 5 m. This error was clearly related to the use of a one-dimensional (1-D) data-interpretation technique which allowed only for very gentle topography along the ice-water interface.

We present an interpretation method for extracting sea-ice keel parameters from AEM data. First we develop an efficient and workable technique for computing the AEM system response over typical keels. The theoretical data are then compiled in the form of a nomogram or look-up table,

Presented at the 57th Annual International Meeting, Society of Exploration Geophysicists. Manuscript received March 17, 1989; revised manuscript received July 21, 1989.

*Department of Engineering Geoscience, 414 Hearst Mining Bldg., University of California at Berkeley, Berkeley, CA 94720.
© 1990 Society of Exploration Geophysicists. All rights reserved.

which in turn serves for the interpretation of the field results. Since no known closed-form analytical expressions exist for computing the electromagnetic (EM) fields of a dipolar source over an indented conducting surface, our approach to this problem is of necessity numerical. To begin with, we describe some background information that is essential for the proper use of airborne electromagnetics in sensing sea-ice thickness.

BACKGROUND INFORMATION

Electrical properties of sea ice and seawater

The electrical conductivity of sea ice depends on its salinity, temperature, structure, and age (Morey et al., 1984). For both first-year and multiyear sea ice, salinity and temperature vary with depth and thus result in a strong vertical variation in electrical conductivity. Kovacs and Morey (1986) also observed that in the ice above sea level, the brine volume is very small. Below sea level, the brine volume increases rapidly with depth, which results in a corresponding increase of the ice conductivity. McNeill and Hoekstra (1973) made measurements on natural sea ice at the frequency of 18.6 kHz at Point Barrow, Alaska. Their results showed that the conductivity of the first-year sea ice increased from about 0.016 S/m near the ice surface to 0.2 S/m at the ice-water interface. For multiyear sea ice this trend was the same, but the conductivity was smaller by more than an order of magnitude. It should be noted here that the conductivity of sea ice is relatively constant over the audiofrequency range from dc to 1 MHz (Addison, 1969; Morey et al., 1984). The electrical properties of seawater are far better established than those of sea ice; seawater's electrical conductivity depends on temperature and salinity (Bullard and Parker, 1970). For seawater under ice cover, seawater conductivity lies in the range of 2.5–3 S/m (Kovacs et al., 1987a).

AEM system

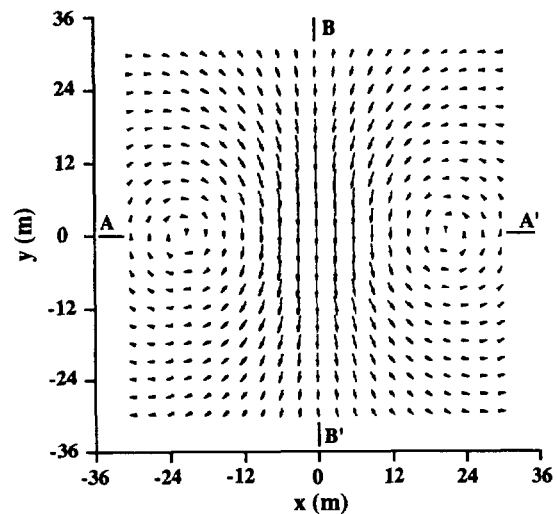
The AEM system considered in this paper is a conventional multicoil instrument used for mineral exploration (Fraser, 1979), which consists of a towed "bird" and the system electronics which is housed in the helicopter. The bird is a rigid fiberglass tube that contains four coil pairs, two of which operate in a horizontal coplanar mode, while the other two operate in a vertical coaxial mode. Each coil pair consists of a transmitter and a receiver that are separated by 6.5 m. In operation, the bird is towed about 30 m below the helicopter, which flies at an altitude of about 60 m, so that the bird is roughly situated 30 m above the ice surface. Each coil pair operates at a distinctive frequency.

The AEM system functions on the principle of EM induction. The transmitter coil is excited by a sinusoidal electric current and produces an alternating magnetic field in space so that currents are induced in any nearby conductors (e.g., seawater). These induced currents in turn produce a secondary magnetic field, which is sensed by the receiver coil and recorded digitally on a magnetic tape. A part of the transmitting current is fed into the recording electronics to cancel the primary magnetic field at the receiver. Using this technique, the secondary field can be measured with high preci-

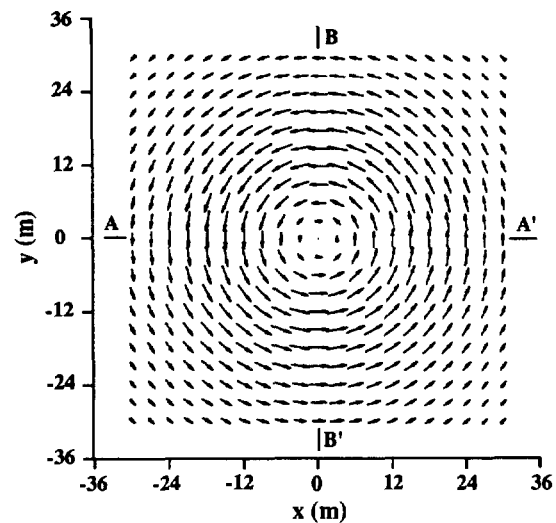
sion, so that its in-phase and quadrature components are recorded in parts per million (ppm) of the primary magnetic field at the receiver with a precision of about 1 ppm. These data are used to determine the height of the bird above the sea-water surface. At the same time, the bird altitude is measured by a laser altimeter installed on the bird. The ice thickness is obtained simply from the difference in these two quantities.

The AEM system footprint

The induced currents on a planar surface of seawater are shown in Figure 1 for a bird height of 30 m above seawater. In this case, for the purpose of giving a quantitative defini-



(a) Horizontal axis dipole transmitter - Co-axial loops



(b) Vertical axis dipole transmitter - Co-planar loops

FIG. 1. Surficial electric currents for (a) coaxial system (x -directed dipoles), and (b) coplanar system (z -directed dipoles). The transmitter is 30 m above the seawater, which is assumed to be infinitely conductive.

tion of the footprint of an AEM system, the seawater is taken to have an infinite conductivity and the sea ice is assumed to be an insulator. The current strength at any point on the water surface is equal in magnitude and orthogonal to the horizontal magnetic field of the image source (Harrington, 1961). The induced currents for a horizontal-axis transmitter coil are symmetrical with respect to the coil plane, and the point of maximum current density is directly below the coil. For a vertical-axis transmitter coil, the induced currents are concentric circles centered at the point directly below the coil center. At the center of the current circles, the current density is zero; the current density peaks along a circle centered below the coil center with a radius of half the bird height over the sea-water surface.

Now, for ease of numerical computation, let us define the footprint of an AEM system as the side of a square surface, centered directly below the transmitter coil, that contains the induced currents which account for 90% of the observed secondary magnetic field. Obviously, for this definition, the footprint depends on the system coil configuration and the bird height. The secondary field from currents within a given square is computed by numerical integration over the square.

The relative contributions to the secondary magnetic field from square regions of different sizes centered below the transmitter are plotted in Figure 2. The abscissa indicates the side length (s) of the square in terms of the bird height (h). For the horizontal axis (x -directed) transmitter, the contribution grows rapidly with increasing square size, since the surface currents are highly concentrated below the square (cf., Figure 1). The contribution overshoots the 100% mark and then decreases because the contributions from the currents outside the square are negative. The footprint of the coaxial system is a square with a side length of 1.35 times the flight height. For a bird height of 30 m, it is a square with 40 m sides. For the coplanar system, the relative contribution grows more slowly with increasing square size than in the coaxial case but increases steadily to reach the 100% mark. The footprint for this system is 3.73 times the flight height or 112 m; it is much larger than that of the coaxial system because, the currents are distributed in a larger area. In

other words, the resolution of the coaxial system along the survey line is better than that of the coplanar system.

Data interpretation for a 1-D model

The goal of data interpretation is to recover the height of the AEM bird over the seawater surface. Subsequently, the ice thickness can be obtained by subtracting the bird altitude above the upper ice surface from this distance. If the ice-water interface relief is mild, a 1-D model can be used to interpret the AEM data. The conventional method for 1-D interpretation relies on the use of an Argand diagram (Grant and West, 1965, p. 550). Since the AEM system response varies with the frequency and with the seawater conductivity, as well as with the flight height, the in-phase and quadrature components of the secondary field are plotted in the form of a nomogram with the conductivity-frequency product and altitude as parameters. Given a measurement of the secondary magnetic field, the bird altitude above the seawater can be readily found from the diagram.

Although this method of data interpretation yields satisfactory values of average ice thickness, it fails to indicate accurately the local ice-keel topography (Kovacs et al., 1987b). The routine interpretation of data acquired in areas of rough ice topography requires at least a 2-D approach based on a rapid method for computing the EM response of an irregular ice-water interface. Finite-element and finite-difference methods, which have been very successfully applied to similar problems (Lee and Morrison, 1985; Stoyer and Greenfield, 1976), are of limited use here because of the associated prohibitive computing costs. In this study, we first develop the required high-speed computational technique, which is used to assemble numerical results needed for the construction of nomograms. These, in turn, are used to interpret AEM field data.

THE FORWARD PROBLEM

Two assumptions are needed to create an algorithm for rapidly computing the AEM system response over irregular sea ice: (1) sea ice is transparent to the EM wave and (2) seawater can be regarded as a perfect conductor. The first assumption is valid in the audiofrequency range, since sea ice is very resistive. The second assumption is reasonable when the system frequency is greater than 30 kHz, so that the skin depth in the seawater is small compared to the ice-keel dimensions. It is shown in the next section, however, that the algorithm using this assumption can also be used for interpreting lower frequency data. The algorithm itself is based on an integral solution of the Neumann boundary-value problem (Graham, 1980) and can be easily implemented using standard numerical methods. For the 2-D case where the ice keel is assumed to have an infinite strike length, the pertinent equations can be transformed into the wavenumber domain by taking a Fourier transform in the strike direction. Once the field is obtained for a range of wavenumbers, the inverse Fourier transform gives the required solution in the space domain. This transformation technique considerably improves the computational speed for the 2-D case.

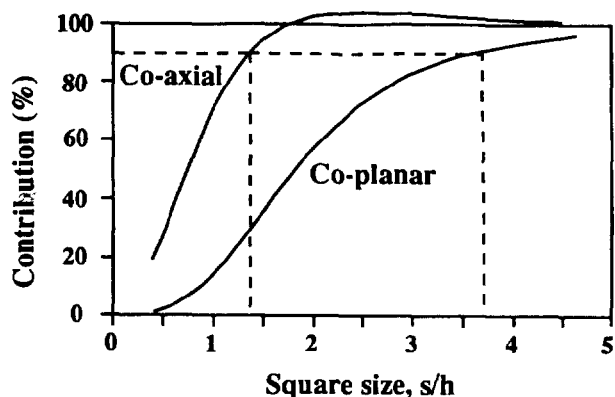


FIG. 2. Contribution to the system response from induced currents as a function of square size. The abscissa is the square side length s normalized by the bird height h .

Neumann formulation for the general case

Consider an alternating magnetic dipole (current loop) source T located in free space as shown in Figure 3. The source is positioned, with arbitrary orientation, over a homogeneous perfectly conductive medium with 3-D surface relief. Electric currents are induced on the surface of the medium, and they give rise to a secondary magnetic field \mathbf{H}_s in free space. The objective here is to calculate this quantity at any point above the surface S .

In the case examined, the height of the source above the medium is small compared to the wavelength, and the observation point is close to the source, so that the EM field is quasi-static. In free space, $\nabla \times \mathbf{H}_s = \mathbf{0}$; and we may relate \mathbf{H}_s to a scalar magnetic potential ϕ ,

$$\mathbf{H}_s = -\nabla\phi. \quad (1)$$

We also have $\nabla \cdot \mathbf{H}_s = 0$ and, correspondingly,

$$\nabla^2\phi = 0. \quad (2)$$

Since the lower medium is assumed to be infinitely conductive, the normal component of the total magnetic field must vanish on S ; i.e.,

$$H_{pn} + H_{sn} = 0. \quad (3)$$

Here H_{pn} and H_{sn} are the normal components of the primary and secondary magnetic fields, respectively. Hence,

$$\left. \frac{\partial\phi}{\partial n} \right|_S = -H_{sn}|_S = H_{pn}|_S. \quad (4)$$

The Laplace equation (2) and the boundary condition (4) constitute the Neumann boundary-value problem. That is, given the normal derivative of the potential on a surface S , we wish to calculate the potential itself above S . Once ϕ is found, \mathbf{H}_s may be calculated from equation (1).

The solution to the Neumann problem outside a closed surface can be expressed as the potential of a fictitious surface charge layer (Graham, 1980)

$$\phi(\mathbf{O}) = \int_S \frac{\xi(\mathbf{P})}{r_{PO}} ds, \quad (5)$$

where $\xi(\mathbf{P})$ is a fictitious magnetic charge density function and r_{PO} is the distance between points \mathbf{P} and \mathbf{O} (see Figure

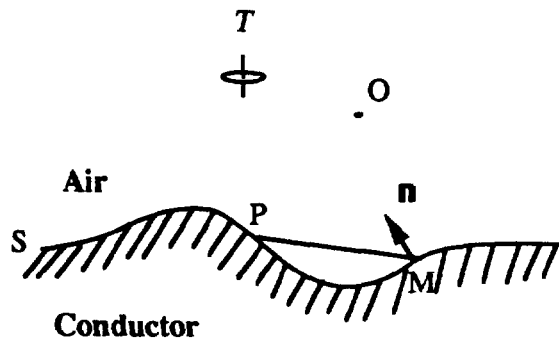


FIG. 3. Model for the Neumann boundary-value problem.

3). The charge density on S satisfies a Fredholm integral equation of the second kind:

$$\xi(\mathbf{M}) = -\frac{1}{2\pi} H_{pn}(\mathbf{M}) - \frac{1}{2\pi} \int_S \xi(\mathbf{P}) \frac{\cos(\mathbf{r}_{PM}, \mathbf{n})}{r_{PM}^2} ds, \quad (6)$$

where $(\mathbf{r}_{PM}, \mathbf{n})$ is the angle between \mathbf{r}_{PM} (the vector connecting \mathbf{P} to \mathbf{M}) and \mathbf{n} (the unit normal vector at \mathbf{M}). In our problem, the surface S extends to infinity. When $\mathbf{r}_{PM} = 0$, the integration kernel has a singularity; but this presents no difficulty in the numerical computation because it is integrable in the sense of its Cauchy principal value.

To solve the integral equation (6), we use the successive approximation method (Mikhlin, 1964). The initial solution (first iteration) is assumed to be the first term on the right-hand side of equation (6); i.e.,

$$\xi(\mathbf{M}) = -\frac{1}{2\pi} H_{pn}(\mathbf{M}).$$

We then use this value in the integral in the equation to compute an improved value of $\xi(\mathbf{M})$, and so on. Once the charge density is known, the secondary magnetic field can be calculated from the following equation, which is obtained by combining equations (1) and (5):

$$\mathbf{H}_s = \int_S \frac{\xi(\mathbf{P})}{r_{PO}^3} \mathbf{r}_{PO} ds. \quad (7)$$

Here \mathbf{r}_{PO} is the vector connecting \mathbf{P} to \mathbf{O} . In the case where S forms a plane, the solution obtained this way can be proven to be identical to that derived from the image principle (Liu, 1989).

Thus, under the quasi-static field assumption, the electrodynamic problem is reduced to a potential-field problem. Frequency is not a parameter, since we assumed perfectly conductive seawater. In fact, this assumption is equivalent to considering the case of the inductive limit. In the computation, the fictitious charge distribution on the surface of the conductive medium is computed first. The secondary magnetic field in free space is then found by summing the contributions from the individual charges, a process analogous to the integral-equation approach for solving the EM scattering problem (Parry and Ward, 1971). In that approach, the equivalent electric and magnetic currents are first sought and the EM fields are then obtained by integrating their contributions.

The two-dimensional case

The ice bottom topography is 2-D when the strike length of the ice keel is much greater than its depth extent and the height of the AEM system above it. Then the relief of the interface is only a function of x ; i.e., $t(x, y) = t(x)$ and the potential of the secondary magnetic field is given by

$$\begin{aligned} \phi(x, y, z) &= \int_{-\infty}^{+\infty} \int_{-\infty}^{+\infty} \frac{\xi(x', y') \sqrt{1 + [dt(x')/dx']^2}}{\sqrt{(x-x')^2 + (y-y')^2 + [z-t(x')]^2}} dx' dy'. \end{aligned} \quad (8)$$

Writing the 2-D equivalent of equation (6), we find that the surface charge density $\xi(x, y)$ satisfies

$$\begin{aligned} \xi(x, y) = & -\frac{1}{2\pi} H_{pn}(x, y) \\ & -\frac{1}{2\pi} \int_{-\infty}^{+\infty} \int_{-\infty}^{+\infty} \xi(x', y') \\ & \times \frac{(x-x')dt(x)/dx - [t(x) - t(x')]}{\{(x-x')^2 + (y-y')^2 + [t(x) - t(x')]^2\}^{3/2}} \\ & \times \left\{ \frac{1 + [dt(x')/dx']^2}{1 + [dt(x)/dx]^2} \right\}^{1/2} dx' dy'. \end{aligned} \quad (9)$$

In equations (8) and (9) the integral with regard to y' is a convolution of the charge density with a geometric kernel. Taking the Fourier transform of both sides, we get

$$\begin{aligned} \Phi(x, k_y, z) = & \int_{-\infty}^{+\infty} \phi(x, y, z) e^{-ik_y y} dy \\ = & 2 \int_{-\infty}^{+\infty} \xi(x', k_y) \sqrt{1 + [dt(x')/dx']^2} K_0(\rho|k_y|) dx' \end{aligned} \quad (10)$$

and

$$\begin{aligned} \xi(x, k_y) = & -\frac{1}{2\pi} H_{pn}(x, k_y) \\ & -\frac{1}{2\pi} \int_{-\infty}^{+\infty} \xi(x', k_y) f(x, x', k_y) dx', \end{aligned} \quad (11)$$

with

$$\begin{aligned} f(x, x', k_y) = & 2 \left\{ \frac{1 + [dt(x')/dx']^2}{1 + [dt(x)/dx]^2} \right\}^{1/2} \\ & \times \frac{(x-x')dt(x)/dx - [t(x) - t(x')]}{\rho'} \\ & \times |k_y| K_1(\rho'|k_y|). \end{aligned} \quad (12)$$

In the above equations,

k_y = angular wavenumber in the y direction,

$\rho = \sqrt{(x-x')^2 + [z - t(x')]^2}$,

$\rho' = \sqrt{(x-x')^2 + [t(x) - t(x')]^2}$,

$K_0(\rho|k_y|)$ = modified Bessel function of zeroth order, second kind, and

$K_1(\rho|k_y|)$ = modified Bessel function of first order, second kind.

We have thus simplified the problem by decomposing a 2-D integral equation into a set of 1-D integral equations. For a dipolar source, the normal component of the primary magnetic field $H_{pn}(x, y)$ can be transformed analytically into the wavenumber domain.

Integral equation (11) can be solved for $\xi(x, k_y)$ using a successive approximation method identical to the one sug-

gested above for the general case. This needs to be done at a number of positive k_y harmonics (including $k_y = 0$). The values of $\xi(x, k_y)$ for negative k_y harmonics are easily obtained by noting the symmetry of this function about $k_y = 0$.

Once the charge density is known, the x and z components of the secondary magnetic field may be computed directly from the following equations:

$$\begin{aligned} H_{sx}(x, k_y, z) = & -\frac{\partial \Phi(x, k_y, z)}{\partial x} \\ = & 2 \int_{-\infty}^{+\infty} (x-x') g(x, x', k_y, z) dx' \end{aligned} \quad (13)$$

and

$$\begin{aligned} H_{sz}(x, k_y, z) = & -\frac{\partial \Phi(x, k_y, z)}{\partial z} \\ = & 2 \int_{-\infty}^{+\infty} [z - t(x')] g(x, x', k_y, z) dx', \end{aligned} \quad (14)$$

where

$$g(x, x', k_y, z) = \xi(x', k_y) \sqrt{1 + [dt(x')/dx']^2} \frac{|k_y|}{\rho} K_1(\rho|k_y|).$$

Once the secondary magnetic field is available in the wavenumber domain, its inverse Fourier transform yields the desired result in the space domain.

Numerical details

(a) **General case.**—The computational domain is chosen to be an area on the surface S , centered directly below the transmitter. The projection of this domain onto the XY plane is a square whose size depends on the elevation of the system. From numerical experiments with a model defined by a flat seawater surface, we find that, to obtain an accuracy of 1%, the length of the side of the square must be greater than six times the bird height. As the AEM system advances, we also translate the computational domain so that its center remains directly below the transmitter. In this way, the size of the computational domain is minimized. Next, the computational domain is discretized into small elements. For simplicity we use constant sampling intervals Δx and Δy along the x and y directions, respectively. Usually we set $\Delta x = \Delta y = 3$ m. For a few narrow keels, however, we chose $\Delta x = 1.5$ m. The grid mesh is usually 60×60 , and each element surface is considered to be flat.

Integral equation (6) is first solved for the charge density $\xi(M)$ using the successive approximation method outlined previously. The initial solution is assumed to be the first term on the right-hand side. We then use this value in the integral in the equation to compute an improved value of $\xi(M)$, and so on. This process converges quickly, and convergence is usually achieved within three iterations. The integral in equation (6) is computed by summing the contributions of every element of the surface. Inside each element, the charge density $\xi(x', y')$ is taken to be constant. On each element within five sampling intervals from the point

$M(x, y)$, the element integral is carried out analytically in the y -direction first and then numerically integrated in the x -direction using nine-point Gaussian quadrature (Press et al., 1986). The contribution of the singular element, where the integration point $P(x', y')$ coincides with the observation point $M(x, y)$, is zero, since $\mathbf{n} \cdot \mathbf{r} = 0$ on that flat element surface. For elements five sampling intervals away from the point $M(x, y)$, the element integral is calculated by multiplying the charge density with the value of the kernel at the midpoint of the element.

Once the charge density is obtained, the secondary magnetic field can be computed from equation (7) by summing the contributions of the charges in each element. In this calculation, the integration kernel in equation (7) can be taken as constant in each element, because the receiver is far from the integration point so that the kernel is relatively invariant.

The computation for each source position is done independently. Ideally, to increase the computational efficiency, the computed kernel values of equation (6) should be stored in the computer memory so that their recalculation for different source positions can be avoided. However, this is not done readily, since the required memory (about 40 megabytes) is very large. When the computation is done on an IBM 3090, a 20-point profile of the AEM system response requires about 15 minutes of CPU time.

(b) The 2-D keel.—For a 2-D keel, equation (11) is solved independently for each wavenumber using the successive approximation method. Fifteen such solutions are necessary for good accuracy. The wavenumber k_y is sampled on a logarithmic scale with five points per decade. Except for its initial value of 0, k_y ranges from 10^{-3} to 1. For any k_y value, the ice-water interface is sampled at $\Delta x = 3$ m, and 80 elements are used for better accuracy than is possible in the 3-D case. Unlike the 3-D case, however, most values of the integration kernel can be stored in the computer memory for use in the computation at the next source point, so that only a few new values arising from the translation of the computational domain need to be calculated. This greatly improves the computational efficiency.

Once the charge density is obtained, the horizontal and vertical components of the secondary magnetic field in k_y space can be computed from equations (13) and (14). We then need to take the inverse Fourier transform to get the required final results. Prior to performing the inverse Fourier transform, however, the field values available at logarithmically spaced points in k_y space need to be interpolated to obtain a uniformly spaced set of k_y values by using cubic-spline interpolation. The computation of the AEM response along a 20 point profile takes only 10 s of CPU time on the IBM 3090. This is faster by two orders of magnitude than the general case of a 3-D ice keel discussed above.

Computational check

The numerical solution was checked on a laboratory scale model. Aluminum was used to simulate the infinitely conductive medium at a linear scale of 1:250. A model AEM system was built at the same scale and was "flown" at a field height of 10 m. The system consisted of a coplanar, vertical-

axis transmitter and receiver which operated at 6 kHz. It can be shown, with the use of the well-known EM scale-model relationships (Grant and West, 1965, p. 481), that the choice of linear scale, modeling material, and operating frequency corresponds to a 1 MHz field system flying over the seawater.

Details of the model are shown in Figure 4, which also exhibits the traversed feature. Note the threefold exaggeration of the vertical scale. The cross-section of the indented surface is a Gaussian curve that simulates a smooth ice keel. Its relief is given by

$$t(x) = A \exp\left(-\frac{x^2}{0.361 W^2}\right), \quad (15)$$

where x = distance from the keel center line, A = maximum keel draft, and W = keel width at half-draft. The shape of the keel is invariant along the strike direction. For the simulated field model, A and W were taken to be 3.4 m and 21 m, respectively. We chose this type of surface because it is simply defined by only two input parameters. Furthermore, it is easy to adjust these parameters to simulate a variety of symmetric sea-ice keels. The measurements and numerical calculation results for this model are displayed in Figure 5, which shows an excellent agreement between the numerical and experimental data. Here the system response is plotted at a point located midway between the transmitter and receiver.

DATA INTERPRETATION

We now define the parameters that describe the AEM anomaly associated with a 2-D ice keel and demonstrate how they change with the ice-keel shape. From the numerical model data, we can construct an interpretation chart that relates the anomaly parameters to the keel parameters. Field data are then interpreted using this chart. Finally, the effects of finite strike length are examined to find the limitations of the 2-D interpretation.

AEM system response for typical ice keels

In the neighborhood of an ice keel, the AEM system response shows an excursion from the background level,

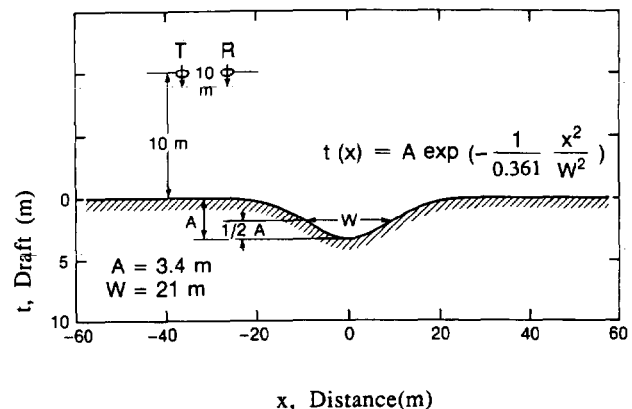


FIG. 4. Coplanar system over a model ice keel. This model was built in the laboratory at a linear scale of 1:250. A = maximum keel draft; W = keel width.

which is called the "anomaly." With reference to Figure 5, let us define the "anomaly amplitude" (labeled C) to be the maximum deviation of the AEM response from the absolute value of the observed background level (labeled B). In order to characterize the shape of the observed anomaly, we define the anomaly width d to be the width of the anomaly at one-half of its maximum value. The anomaly amplitude and width depend not only on the geometry of the ice keel but also on the bird height above the ice-water interface. In order to minimize the influence of factors other than keel geometry, we also use the "normalized anomaly amplitude," which is the anomaly amplitude normalized by the background level (i.e., ratio C/B), and the "normalized anomaly width," which is the anomaly width normalized by the average bird height above the seawater surface.

We now examine the AEM response for 2-D sea-ice keels as a function of their size and shape. For these calculations, the EM system has a coil separation of 6.5 m and is flown 25 m above the flat upper-ice surface. With the exception of the zone containing the keel, the sea ice is 5 m thick and is assumed to have negligible electrical conductivity, while the seawater is taken to be infinitely conductive. Numerical results are then obtained for both the coaxial and the coplanar systems. The keel is assumed to have the shape of a Gaussian curve shown in Figure 4 and defined by equation (15).

Figure 6 shows the coaxial and coplanar system responses for two different keels with parameters $A = 12$ m and $W = 28$ m and 14 m. Here H_x is the coaxial system response, while H_z is the coplanar system response. Each system response shows a large anomaly related to the model ice keels. For a keel width W of 28 m, the coaxial anomaly amplitude is

205 ppm, which is 35% of the background value. The anomaly width d in this case is 45 m. When the keel width is halved to 14 m while the other parameters are kept fixed, the coaxial system anomaly is reduced significantly. Here the anomaly amplitude decreases by 37% to 130 ppm and the anomaly width decreases by 33% to 30 m. From a comparison of the coaxial and coplanar anomalies (Figure 6), we can see that the coplanar system response shows similar behavior, but note that the coplanar system anomalies are much broader.

To demonstrate the failure of 1-D interpretation, we interpreted the synthetic 130 ppm coaxial anomaly using the Argand diagram method. The bird height was found to be 33 m, but since the bird height over the flat part of the seawater surface was 30 m, the interpreted keel draft is then 3 m. The actual keel draft at this point, however, is 12 m. In this case, the interpreted thickness is only 25% of the model ice thickness.

Next, the keel draft A is halved to 6 m, while the keel width is kept constant at $W = 28$ m. The corresponding system response is shown in Figure 7. In this case, the coaxial anomaly amplitude contracts by 29%, but the corresponding decrease in the anomaly width is only 8%. Similarly, for the coplanar system, the anomaly amplitude drops by 37%, but the anomaly width decreases by only 3%. Thus, we find that the anomaly amplitude is sensitive to both the thickness and the width of the keel. It is essentially a function of the area of the cross-section of the keel. In contrast, the anomaly width is related primarily to the keel width. It is much less sensitive to the keel thickness as long as the shape of the keel does not change.

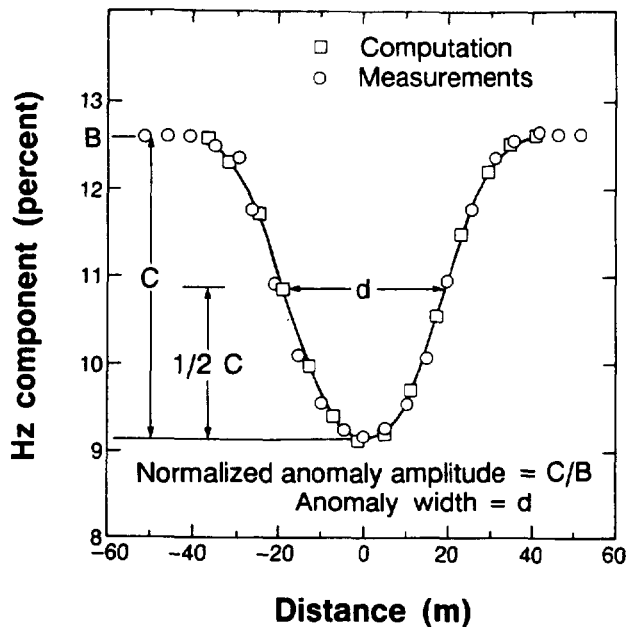


FIG. 5. Comparison of scale-model measurements and the numerical solution for the model shown in Figure 4. B = background response; C = anomaly amplitude. 1% = 10^4 ppm.

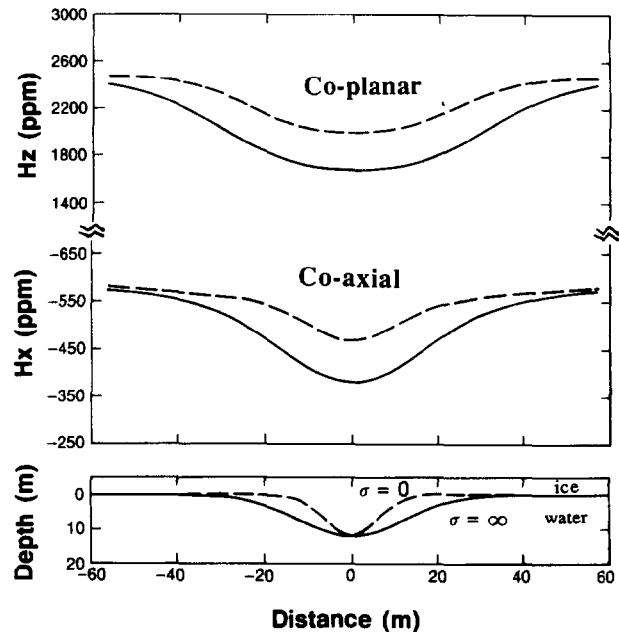


FIG. 6. System response (top) for model ice keels (bottom) with parameters $A = 12$ m, $W = 14$ m (dashed lines) and $W = 28$ m (solid lines). H_x and H_z indicate the coaxial and coplanar system responses, respectively.

Interpretation chart

To interpret field data, we need a strategy to relate the observed EM anomaly to the keel geometry. In terms of the smooth keel used in our analysis, we wish to estimate the two keel parameters A and W from the observed anomaly parameters. This can be done with the aid of a nomogram that is constructed from a complete set of normalized anomaly-amplitude and anomaly-width values computed for a variety of model keels defined by a systematic set of A and W parameters. The required interpretation chart for the coaxial system response is shown in Figure 8. The vertical axis of the chart defines the normalized anomaly amplitude C/B (cf., Figure 5), while the horizontal axis represents the normalized anomaly width d/h . The two sets of parametric curves intersect each other at good angles and are well separated. The solid curves correspond to constant values of the draft A , while the dashed ones are related to constant values of keel width W . The displayed values of a and w are the keel draft A and width W normalized by h , the average bird height above the seawater surface away from the keel. As shown, the normalized anomaly amplitude decreases with the decrease of the keel draft and keel width. In fact, the line for $a = 0.8$ rapidly tends to zero and intersects the lines $a = 0.4$, $a = 0.2$, etc. For purposes of clarity, this overlap is not shown in Figure 8. It does not pose a serious problem in practice, since such narrow and sharp keels are highly improbable. Although the interpretation chart is constructed for $h = 30$ m, it can be used for the range $h = 25$ m–50 m with an error less than $\pm 4\%$. A parallel analysis can also be carried out for the coplanar system (Liu, 1989).

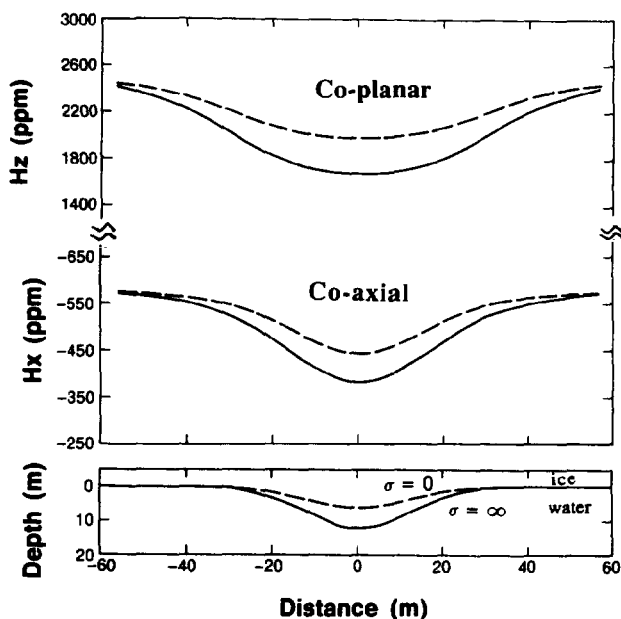


FIG. 7. System response (top) for model ice keels (bottom) with parameters $A = 6$ m (dashed lines) and $A = 12$ m (solid lines), $W = 28$ m. H_x and H_z indicate the coaxial and coplanar system responses, respectively.

Interpretation of field data

As pointed out previously, the interpretation chart shown in Figure 8 is constructed using the perfect-conductor model. In this case, the system response has only an in-phase component. However, it has been shown that the anomaly shape for data above 2 kHz is close to that in the inductive limit (Liu, 1989). This makes the interpretation chart shown in Figure 8 applicable for a wide range of frequencies. However, note that the lower the frequency, the smaller the normalized anomaly amplitude, resulting in an underestimation of the ice-keel draft; this error is less than 10% for data above 2 kHz (Liu, 1989).

We now consider AEM field data collected over an ice keel in Prudhoe Bay in 1985 (Kovacs et al., 1987b). Part of the 4160 Hz (coaxial) data for line F6L3 are shown in Figure 9. Note that the in-phase and quadrature responses are plotted at different scales. The altitude is the distance from the system boom to the ice surface measured by a laser altimeter. As expected, the data are highly correlated with altitude. We first interpreted the data using a 1-D technique with a result that shows a 3.09 m average ice thickness but gives no indication of the ice keel (solid squares in Figure 9c). This result confirms an independent 1-D analysis of the same data performed by Kovacs et al. (1987b). We note, however, that an anomaly in the system response can be seen between fiducials 2668–2675. Assuming that it is not related to the small altitude variation in that area, we find that the anomaly width d is 32 m and that the normalized anomaly amplitude is 6.5%. Since h is about 39 m (altitude + average ice thickness), the normalized width $d/h = 0.82$. The corresponding point is found in the interpretation chart (point D in Figure 8), which gives $a = 0.08$ and $w = 0.42$. Hence, $A = a \times h = 3.08$ m, $W = w \times h = 16.2$ m. The interpreted keel is plotted symmetrically about the point of maximum anomaly in Figure 9c (dashed line). The solid line in that illustration indicates the average of the drill-hole measurements made along three parallel lines 11.5 m apart

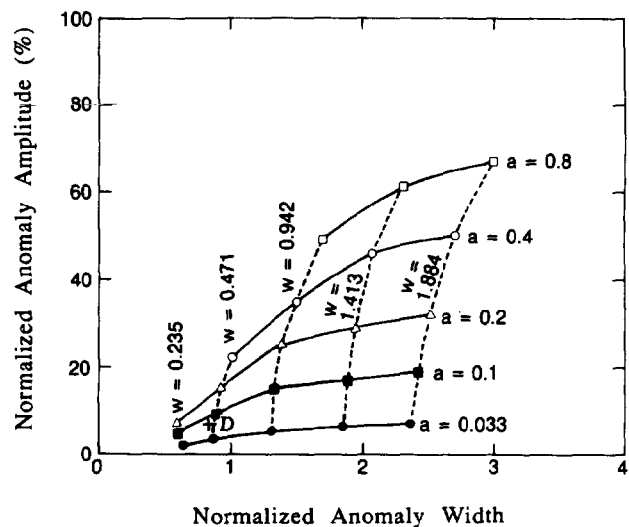


FIG. 8. Interpretation chart for coaxial system response. a and w are the maximum keel draft and the keel width normalized by the bird height h .

beneath the flight path. As we can see, the interpreted keel is a good approximation to the existing feature.

Effects of keel strike extent

In order to define one of the limitations of the 2-D interpretation method, it is worthwhile to consider the effects of finite keel strike extent. To do this, we compute the AEM anomaly for a 3-D Gaussian keel whose draft is given by

$$r(x, y) = A \exp \left(-\frac{y^2}{0.361 L^2} - \frac{x^2}{0.361 W^2} \right). \quad (16)$$

Here the keel strike extent L is defined in the same way that we previously defined the keel width W . To demonstrate the influence of this parameter, we examine its effect on a shallow keel described by $A = 3$ m, $W = 24$ m, and a series of L values which range from 12 m to 96 m. The results of these calculations for a central profile flown at 25 m above the ice are shown in Figure 10. For the purpose of comparison, it also includes the numerical results for an infinitely long (2-D) keel.

It appears from the results shown in Figure 10 that a keel strike of about 96 m or about three times the bird altitude over the ice-water interface is required if the 2-D interpretation method is to be used with an error of less than 10%. Surprisingly, this conclusion holds for both the coaxial and the coplanar systems, even though their footprints differ widely from each other.

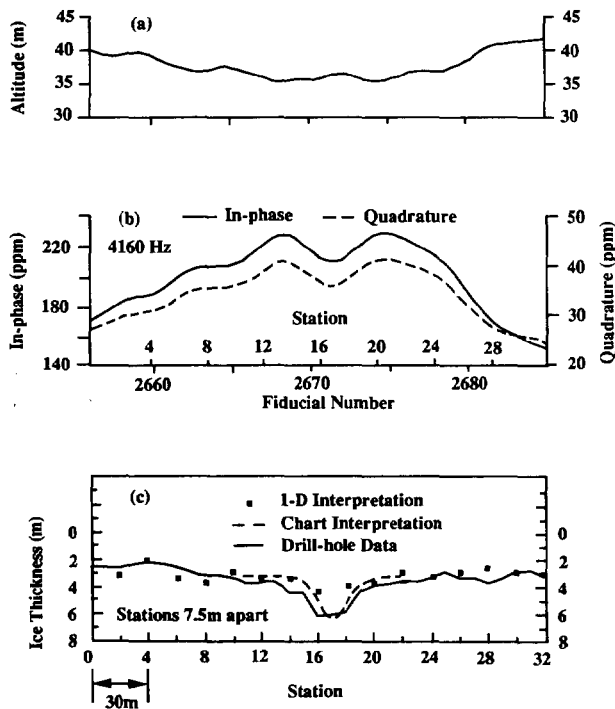


FIG. 9. Prudhoe Bay field data and interpreted result. (a) Bird altitude, (b) 4160 Hz coaxial system data, and (c) interpreted and measured keel outline.

CONCLUSIONS

From the distribution of the induced currents on the seawater surface, we see that the horizontal dipole transmitter used in the coaxial system produces a more concentrated current pattern than does the coplanar system. This results in a smaller footprint for the coaxial system; hence, the coaxial system configuration may have better resolution than its coplanar equivalent. Nevertheless, both systems are equally sensitive to ice-keel strike extent.

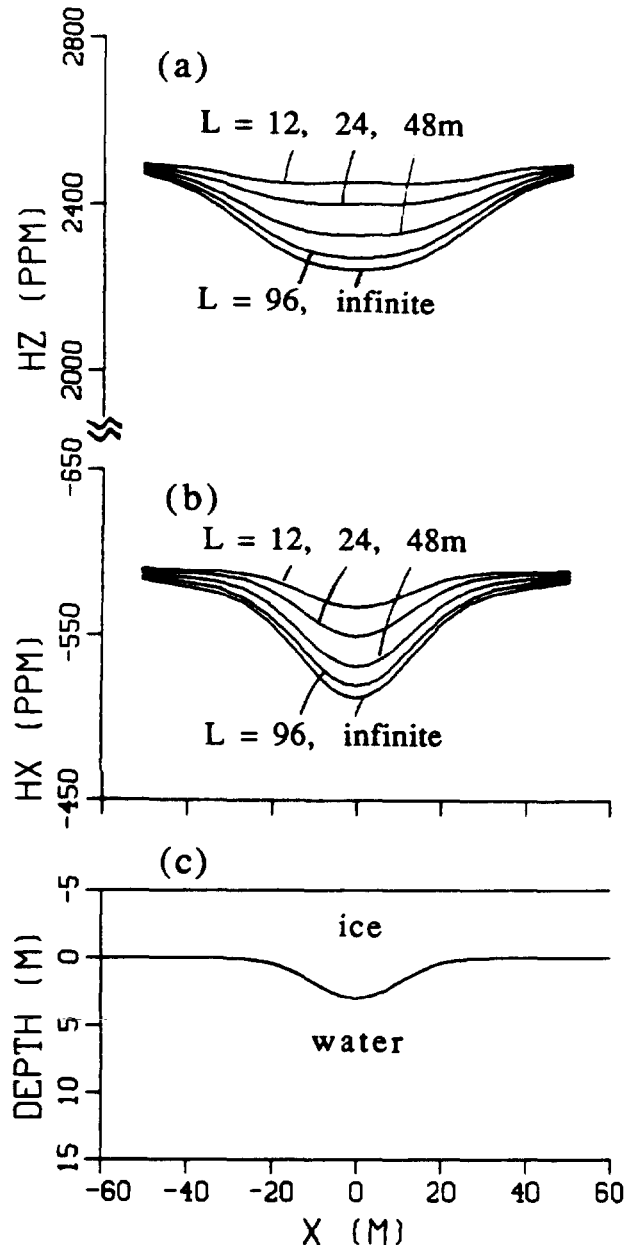


FIG. 10. System response for 3-D model ice keels with parameters $A = 3$ m and $W = 24$ m; bird height above upper ice surface = 25 m. (a) Coplanar system response, (b) coaxial system response, and (c) cross-section of the ice keel.

The problem of simulating AEM data acquired in areas of sea-ice pressure ridges and keels is best formulated as a Neumann boundary-value problem and is solved using the integral equation approach. For 2-D ice keels, the pertinent equations can be transformed into the wavenumber domain by taking the Fourier transform along the strike direction. The resultant equations admit a very efficient numerical solution.

The AEM anomaly size is a function of both the thickness and the width of the keel, and thus essentially depends on the area of the keel's cross-section. In contrast, the anomaly width is related primarily to the keel width. It is much less sensitive to the keel draft, as long as the shape of the keel remains invariant. Although the anomaly size can be large, the 1-D model hypothesis is inadequate for the interpretation of the data collected over a typical ice keel.

By compiling numerical data for 2-D Gaussian model keels, we have constructed an interpretation chart. When the keel strike length is more than three times the flight height of the AEM system, the chart can be used to estimate accurately the size and shape of an ice keel from the associated AEM anomaly. Note here that, to apply the chart interpretation, the variation of the system altitude should be smaller than the feature one is detecting. Although the chart is constructed from model data obtained in the inductive limit, it can be used to interpret lower frequency data, because the anomaly shape and relative amplitude are not overly dependent on the frequency once that frequency is chosen to lie in the upper audio range.

ACKNOWLEDGMENTS

This work was partially funded by ARCO Oil and Gas Company under contract no. (M-417) (AR-78695), the Cold Regions Research and Engineering Laboratory (CRREL) of the U.S. Army under contract no. DACA89-85-K-0008, and the Naval Oceans Development and Research Activity (NORDA) under contract no. N00014-87-K-6005.

REFERENCES

Addison, J. R., 1969, Electrical properties of saline ice: *J. Appl. Phys.*, **40**, 3105-3114.

Becker, A., Morrison, H. F., and Smits, K., 1983, Analysis of

airborne electromagnetic systems for mapping thickness of sea ice: NORDA technical note 261.

Bullard, E. C., and Parker, R. L., 1970, Electromagnetic induction in the oceans, in Maxwell, A. E., Ed., *The sea*, **4**: Wiley-Interscience, 695-730.

Fraser, D. C., 1979, The multicoil II airborne electromagnetic system: *Geophysics*, **44**, 1367-1394.

Graham, I. G., 1980, Some application areas for Fredholm integral equations of the second kind, in Anderssen et al., Ed., *The application and numerical solution of integral equations*: Sijthoff and Noodhoff Internat. Publ., 75-101.

Grant, F. S., and West, G. F., 1965, *Interpretation theory in applied geophysics*: McGraw-Hill Book Co.

Harrington, 1961, *Time-harmonic electromagnetic fields*: McGraw-Hill Book Co.

Harwood, T. A., 1971, The reasons for seeking to make thickness measurements by remote sensing: Proceedings of a seminar on thickness measurement of floating ice by remote sensing, DREO tech. note no. 71-14, Defence Research Board of Canada.

Holladay, J. S., Valteau, N., and Morrison, E., 1986, Application of multi-frequency helicopter electromagnetic surveys to mapping of sea-ice thickness and shallow-water bathymetry, in Palacky, G. J., Ed., *Airborne resistivity mapping*: Geol. Surv. of Canada, 91-98.

Kovacs, A., and Morey, R., 1986, Electromagnetic measurements of multi-year sea ice using impulse radar: *Cold Regions Science and Technology*, **12**, 67-93.

Kovacs, A., Morey, R. M., and Cox, G. F. N., 1987a, Modeling the electromagnetic property trends in sea ice, Part I: *Cold Regions Science and Technology*, **14**, 207-235.

Kovacs, A., Valteau, N., and Holladay, J. S., 1987b, Airborne electromagnetic sounding of sea-ice thickness and sub-ice bathymetry: *Cold Regions Science and Technology*, **14**, 289-311.

Lee, K. H., and Morrison, H. F., 1985, A numerical solution for the electromagnetic scattering by a two-dimensional inhomogeneity: *Geophysics*, **50**, 466-472.

Liu, G., 1989, Airborne electromagnetic sensing of sea-ice thickness: Ph.D. thesis, Univ. of Calif. at Berkeley.

McNeill, D., and Hoekstra, P., 1973, In-situ measurements on the conductivity and surface impedance of sea ice at VLF: *Radio Sci.*, **8**, 23-30.

Mikhlin, S. G., 1964, *Integral equations*: Pergamon Press, Inc.

Morey, R. M., Kovacs, A., and Cox, G. F. N., 1984, Electromagnetic properties of sea ice: *Cold Regions Science and Technology*, **9**, 53-75.

Parry, J. R., and Ward, S. H., 1971, Electromagnetic scattering from cylinders of arbitrary cross-section in a conductive half-space: *Geophysics*, **36**, 67-100.

Press, W. H., Flannery, B. P., Teukosky, S. A., and Vetterling, W. T., 1986, *Numerical recipes*: Cambridge Univ. Press.

Stoyer, C. H., and Greenfield, R. J., 1976, Numerical solutions of the response of a two-dimensional earth to an oscillating magnetic dipole source: *Geophysics*, **41**, 519-530.